Two-Dimensional Optical Beam Steering With InP-Based Photonic Integrated Circuits

Weihua Guo, Pietro R. A. Binetti, Chad Althouse, Milan L. Mašanović, *Member, IEEE*, Huub P. M. M. Ambrosius, Leif A. Johansson, *Member, IEEE*, and Larry A. Coldren, *Fellow, IEEE*

(Invited Paper)

***Abstract*—Two-dimensional optical beam steering using an InP photonic integrated circuit has been demonstrated. Lateral beam steering controlled by a 1-D phased array has been made easier through on-chip interferometer monitors. Longitudinal beam steering controlled by the input wavelength has demonstrated an efficiency of 0.14 °/nm. Very fast beam steering ($>10^7$ °/s) in both dimensions has been demonstrated as well. As the latest development, a widely tunable sampled-grating distributed Bragg reflector laser has been monolithically integrated and 2-D beam steering has been demonstrated with this on-chip tunable laser source.**

***Index Terms*—Light detection and ranging (LIDAR), optical beam steering, optical phased array (OPA), photonic integrated circuits (PICs).**

I. Introduction

ELECTRONICALLY controlled optical beam steering is potentially useful for a number of applications such as light detection and ranging (LIDAR), free space secure laser communication, printing, etc. Various methods have been demonstrated to achieve this goal. One typical method is the optical phased array (OPA), which is used for 1-D optical beam steering [1]. Different material systems have been used to realize OPAs such as liquid crystal [2] and GaAs [3].

To achieve 2-D optical beam steering, the most natural implementation might be to mimic the active electronically scanned array which consists of a 2-D array of transmitters and receivers. It is used for 2-D RADAR scanning [4]. A 2-D array of optical emitters such as a 2-D vertical-cavity-surface-emitting-laser (VCSEL) array can be used as the transmitter in this approach. Making lasers in the array coherent to each other is essential for optical beam steering. This has been demonstrated by the way of injection locking [5] or adjacent laser coupling [6]. Also needed by this approach is a 2-D array of phase shifters. Each phase shifter in the array should ideally be able to generate 2π phase change. This, however, is very challenging.

A two-dimensional microelectromechanical system (MEMS) array has also been used for 2-D optical beam steering [7], however achieving high-speed and large-angle beam steering simultaneously is a big challenge for this scheme.

Recently, there has been a demonstration of using wavelength tuning to steer the optical beam in one dimension through waveguide dispersion [8]. This is essentially similar to using surface-emitting gratings, in which the emitting angle depends on the input wavelength. By combining 1-D OPA with surface-emitting gratings, 2-D optical beam steering has been realized [9]. The benefit of this scheme is that the beam steering in one dimension is only controlled by one variable, i.e., the wavelength, so the entire control is much simpler. The OPA has been demonstrated to be controlled by using a single triangular contact as well [9].

Recently, the authors demonstrated 2-D optical beam steering with an InP photonic integrated circuit (PIC) using the scheme of 1-D OPA plus wavelength tuning with surface-emitting gratings [10]. However, instead of using one triangular pad, individual pads for each single channel in the OPA were used. Analogous efforts by our coworkers on the silicon-on-insulator platform have also been carried out and similar results have been demonstrated [11]. This approach does increase the number of controls needed, but allows large tolerances for device fabrication because the phase errors due to imperfect fabrications of the channel waveguides can be compensated by the individually controlled phase shifters.

Also, the overall phase needed to be generated is much less compared to the single triangular pad because modulo of 2π for phase can be used. In other words, it is not needed to generate more than 2π phase change for a single channel, which is not the case for the triangular pad. Considering that in InP, a phase change induced by current injections is always associated with some amount of loss, less phase change also means less loss.

We chose the InP platform for the integration because of several reasons: first, InP is a very mature platform for large-scale photonic integration [12], and various active–passive devices, such as widely tunable lasers, have been implemented in it; therefore potentially all components necessary for 2-D beam steering can be integrated on a single PIC; second, in InP, semiconductor optical amplifiers (SOAs) can be integrated to boost

Manuscript received November 1, 2012; revised December 31, 2012; accepted December 31, 2012. This work was supported by the DARPA SWEEPER Program.

W. H. Guo, P. R. A. Binetti, M. L. Mašanović, L. A. Johansson, and L. A. Coldren are with the Department of Electrical and Computer Engineering, University of California Santa Barbara, CA 93106 USA (e-mail: guow@ece.ucsb.edu; pbinetti@ece.ucsb.edu; mashan@ece.ucsb.edu; leif@ece.ucsb.edu; coldren@ece.ucsb.edu).

C. Althouse was with the Department of Electrical and Computer Engineering, University of California Santa Barbara, CA 93106 USA. He is now with Innovative Micro Technology, Goleta, CA 93117 USA (e-mail: althouse@umail.ucsb.edu).

H. P. M. M. Ambrosius is with the Department of Electrical Engineering, Eindhoven University of Technology, 5600 MB Eindhoven, The Netherlands (e-mail: H.P.M.M.Ambrosius@tue.nl).

Color versions of one or more of the figures in this paper are available online at http://ieeexplore.ieee.org.

Digital Object Identifier 10.1109/JSTQE.2013.2238218

1077-260X/$31.00 © 2013 IEEE

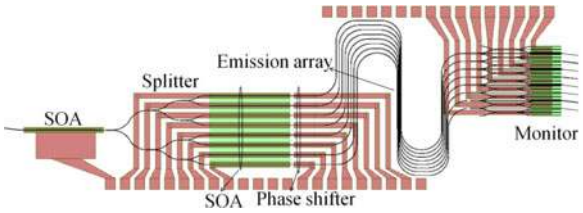

Fig. 1. Layout of the PIC.

the optical power, so that potentially the PIC can generate high optical power which is essential for LIDAR applications; third, the phase shifters in InP with current injections can have up to a gigahertz bandwidth, the tuning speed of the widely tunable laser, such as the sampled-grating distributed Bragg reflector (SGDBR) laser [13], can reach a few nanoseconds [14], so potentially an InP PIC can achieve very fast optical beam steering.

The rest of this paper is organized as follows: the PIC layout and processing are introduced in Sections II and III, respectively; Section IV introduces the PIC test in detail including the following subsections: test setup, contact to the PIC and bias control, beam steering controlled by phase shifters, beam steering controlled by wavelength tuning, 2-D beam steering, and fast beam steering; Section V introduces the latest development where a widely tunable SGDBR laser is monolithically integrated; the summary is given in Section VI.

II. PIC Layout

The PIC layout is shown in Fig. 1. From left to right, the PIC contains an SOA preamplifier, a 1×8 splitter consisting of cascaded 1×2 multimode interferometers (MMIs) which splits the input into eight equal channels, an array of eight SOAs, an array of eight phase shifters, bends, emission array, and the monitor array. All the SOAs are 800 μm long and 2.7 μm wide. All the phase shifters are 200 μm long and 2.7 μm wide. The emission array consists of eight uniformly spaced waveguides. Buried second-order gratings are used for the surface emission. The gratings are 500 μm long and the waveguide spacing is 5.5 μm which is chosen to ensure that the final beamwidth (full-width at half-maximum—FWHM) will be within 2°. The waveguide gap in the emission array is thus 2.8 μm which makes the crosstalk between waveguides negligible when deeply etched ridge waveguides are used. As seen from Fig. 1, the bends used in each channel are the same: the same radius of 200 μm and the same total bending angle of 1.5π. These bends are added to make each channel have the same total length. They are needed because the SOA array has a spacing of 100 μm which is much larger than the spacing in the emission array.

The detailed structure of the monitor array is shown in Fig. 2(a) and (b). Each channel is split into three equal parts through a 1×3 MMI. The central part outputs directly for possible far-field analysis. The two neighboring parts from two adjacent channels are combined by a 2×1 MMI with the output entering into a photodiode which is 5 μm wide and 200 μm long. Two more waveguides are added at the output interface of the 2×1 MMI sandwiching the central output as seen from Fig. 2(b). When the two inputs of the 2×1 MMI have a π

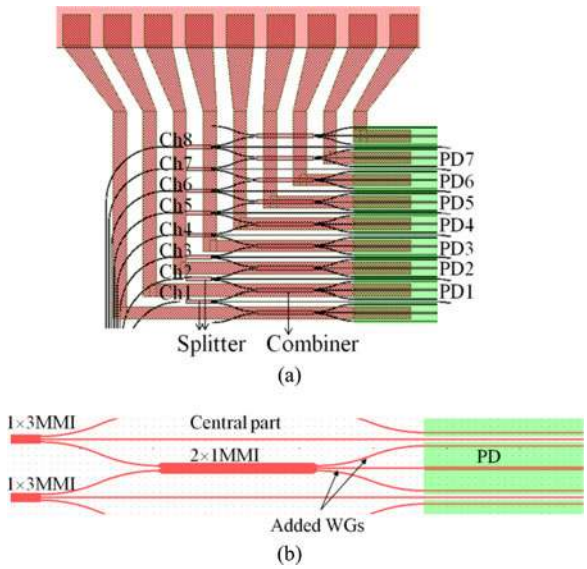

Fig. 2. Blow-up of (a) the monitor array and (b) a single channel of the monitor array.

phase difference, they will interfere destructively at the output interface of the MMI. Two spots will be formed at the entrance of the two added waveguides and will be guided away so that they do not enter into the central output waveguide. The interference extinction ratio is thus increased. From Fig. 2(a) and (b), it can be seen that two adjacent channels form interferometer structures with the interference monitored by the on-chip photodiodes. These monitors can help to characterize the phase shifters in each channel on-site. This point will be explained in detail in Section IV.

In this first experiment, the input signal was fiber coupled from an off-chip SGDBR widely tunable laser into the PIC. As our latest development, an SGDBR has been monolithically integrated which has demonstrated similar results [15] (see Section V). The SGDBR laser contains the back mirror section, phase section, gain section, front mirror section, and the output SOA section. In our practical measurement, the gain section and the front SOA section are biased with fixed currents. Different current sources are used to control the bias to the front and back mirror sections separately so as to tune the laser. The phase section is left floated. In the following tuning experiment, we mainly show the supermode selection of the laser. But it is known that by controlling the current injected into the mirrors and the phase section in a coordinated way, the laser can be tuned to any wavelength covered by its quasi-continuous tuning range [13].

III. PIC Fabrication

To realize the passive–active integration required by the PIC, the quantum-well intermixing (QWI) technology is employed [16]. A base epi-structure as shown in Fig. 3(a) has been used. The waveguide core includes the upper and lower optical confinement layers which are 105-nm-thick InGaAsP material with a bandgap of 1.3 μm (1.3Q), and quantum wells (QWs) (ten wells, 6.5 nm thick with 0.9% compressive strain; 11 barriers, 8.0 nm thick with 0.2% tensile strain; the QWs have a

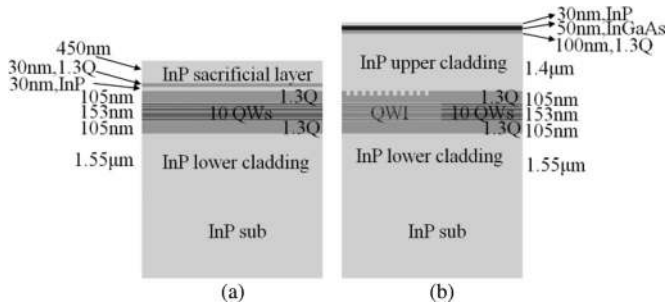

Fig. 3. (a) Base epi-structure. (b) Wafer structure after regrowth.

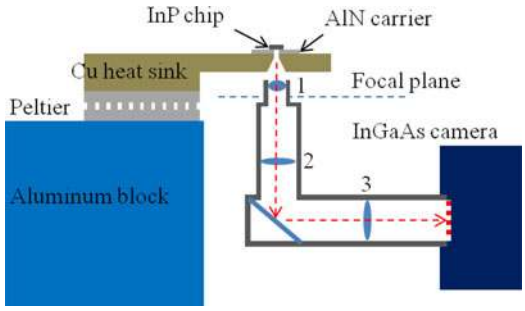

Fig. 4. Schematic of the measurement setup.

photoluminance peak at 1.54 μm). The top 450-nm-thick InP is sacrificial and is used for phosphorus ion implantation. The implantation will form a shallow surface layer with defects on the wafer. Rapid thermal annealing afterward is used to drive vacancies created by the point defects down through the QWs which cause atoms to interdiffuse between the wells and barriers and cause the bandgap of the QWs to increase so as to become transparent to the emission of the QWs without intermixing.

After the QWI step, the sacrificial InP layer and the 1.3Q etching stop layer are removed through selective wet etching. Then, second-order gratings for emission are patterned through E-beam lithography. The gratings are etched 20 nm into the 1.3Q upper optical confinement layer through the reactive ion etching with a gas combination of $CH_4/H_2/Ar$. After the grating step, one time blanket regrowth is used to finish the whole wafer structure. The regrowth structure is shown in Fig. 3(b). It can also be seen that the grating is formed in the passive waveguide region.

After the whole wafer structure has been finished, waveguides are patterned using an I-line stepper. Two layers of hard masks are used: 70-nm Chrome and 600-nm SiO_2. The etching of InP is carried out by inductively coupled plasma through a gas combination of $Cl_2/H_2/Ar$. Optimized etching condition ensures a very smooth and vertical sidewalls of the waveguides [17]. For processing simplicity, deep ridge waveguides (about 5 μm) are used for both passive and active waveguides. This is not ideal for active waveguides because of surface recombination and weakened thermal dissipation. It would be ideal to use surface ridge waveguides for those active waveguides. Then, surface-deep ridge transitions with low loss and low reflection will have to be used, which however will make the processing much more complex [12].

After the waveguides are formed, 350-nm SiN_x is deposited for electrical isolation; then, P-vias are opened and Pt/Ti/Pt/Au P-contact metal is deposited through the liftoff process. The SiN_x on top of the waveguides in the emission array is removed as well, but there is no metal deposited on top. The InP protection layer on the waveguide top is wet etched right before the metal deposition, which is beneficial to reduce the contact resistance. Considering that in the structure metal wires cross waveguides at many places as seen from the layout in Fig. 1, photosensitive benzocyclobutene (BCB) is spin on top of the wafer to planarize. The vias for those metal contacts are opened simply through exposure and development of the BCB. The BCB on top of the waveguides in the emission array has been removed as well. After curing BCB, 200-nm SiN_x is deposited on top of the wafer. This SiN_x layer has twofold functions: one is to help the later deposited pad metal to stick and the other is to act as an antireflection coating layer for the emission array. The final step for the top-side processing is depositing the Ti/Au thick metal stack for pads and the wires leading to the pads. After thinning the wafer down to approximately 100 μm, the N-contact metal is deposited on the backside of the wafer.

The grating emits vertically both upward and downward. Theoretical calculation [18] and practical measurement using a larger area (5 mm $\times$ 5 mm) Germanium detector show that the powers radiated upward and downward are approximately equal to each other. In the following measurement, only the downward emission is imaged, as will be shown in Section IV. So an aperture has to be opened through the backside metal and has to be aligned with the emitting gratings. This is achieved through a liftoff process and an infrared contact aligner. After the whole process, the PIC is cleaved and mounted onto an AlN carrier facing up. Because the emission is downward, there is a hole opened in the AlN carrier as well. This hole is aligned to the emission window in the backside metal of the PIC during the soldering process with a flip-chip bonding machine. The PIC on carrier is now ready for test. The final finished PIC is approximately 6 mm long and 2 mm wide.

The passive waveguide loss and the active waveguide gain are tested through some test structures fabricated with the PIC at the same time. A loss level of approximately 2.0 dB/mm is observed. The active waveguide can have a maximum gain reaching 35 dB/mm at the current density of 9 kA/cm^2. The maximum power that can be generated by a single SOA is approximately 20 mW under the dc driving condition. The 200-μm-long phase shifter is able to generate 2π phase change with a current injection less than 20 mA. The additional loss associated with 2π phase change is approximately 1.5 dB.

IV. PIC Test

A. Test Setup

A schematic of the measurement setup is shown in Fig. 4. Three lenses installed in lens tubes are used for the far-field imaging. The first lens with the smallest focal length (10 mm) and the highest numerical aperture (0.55) is used to capture the emission from the PIC as much as possible. The closer the lens to the PIC, the larger the angle range it can capture. The far-field pattern of the emission is generated on the lower focal

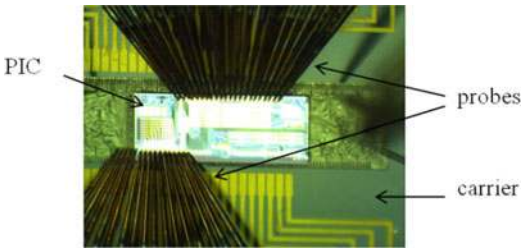

Fig. 5. Microscope image of the PIC on the setup contacted by multiprobes.

plane of the first lens. Another two lenses are used to project the far-field pattern onto the image plane of the InGaAs camera with a low level of magnification. The effective focal lengths of the second and third lenses are 75 and 100 mm, respectively. The camera has a 2-D array of pixels with 25-μm pitch in both dimensions and the array size is 320 $\times$ 256. This determines that our imaging system has the ability to resolve the far field with the angle range of 34.8° $\times$ 27.7° and the angle resolution is 0.1° in both dimensions.

B. Contact to the PIC and Bias Control

As seen from Fig. 4, the PIC is soldered onto an AlN carrier first and then the carrier is placed onto a copper heat sink. The emission is downward, so there is a tapered hole in the part hanging off the heat sink which is aligned with the hole in the carrier. The temperature is controlled through a Peltier and a thermistor which is embedded in the heat sink close to the carrier. In our measurement, the temperature is controlled at 16 °C.

To make contacts to the PIC, two multiprobes are used to probe the pads on the PIC directly. A microscope image in Fig. 5 shows the probes contacting the pads. The first thing normally done is to measure the *I–V* curves of all the diodes on the PIC to check if they work. The single PIC has nine SOAs, eight phase shifters, and nine photodiodes. It is not difficult to find a PIC with all the diodes working after processing. The typical series resistance is around 5 Ω. Normally, the preamplifier SOA is biased through a current source and the eight-SOA array is biased through another voltage source. To account for the variation of the SOA series resistance, each SOA is connected with a variable resistor (variable range from 0 to 50 Ω) and a fixed 10-Ω resistor.

A schematic of the connections is shown in Fig. 6. First the variable resistor is maximized and the voltage output from the voltage source is fixed at 4 V. Then, the variable resistor is adjusted and the voltage drop upon the 10-Ω fixed resistor is monitored to find out the current. When the voltage drop is 1 V, the adjustment is stopped. This means that the current injected into the corresponding SOA is 100 mA. The adjustment to each channel is made in sequence. Because the shared connections between channels have resistance as well, when one channel is adjusted, the other channels are slightly influenced. This process is repeated several times until all of the channels have a current of approximately 100 mA. The eight phase shifters are biased independently through the current outputs of a 16-bit DAC card.

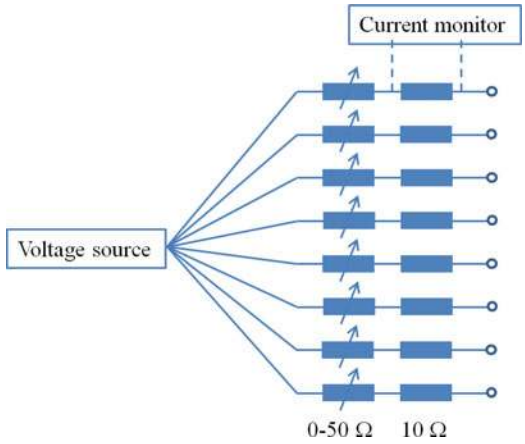

Fig. 6. Variable resistance network connected to the SOA array.

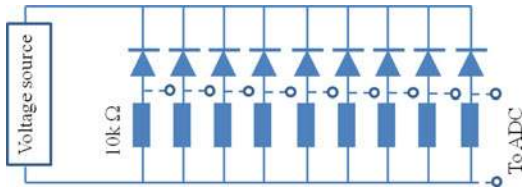

Fig. 7. Connections to the monitor photodiode array.

The current output range from the DAC card is from 0.1 to 20.2 mA. The nine monitor photodiodes are reverse biased by a single voltage source at −2 V through a connection sketched in Fig. 7. The connected series resistance is 10 kΩ. The voltage drops through the resistances is monitored by an ADC card.

C. Beam Steering Controlled by Phase Shifters

As introduced previously, the scheme of 1-D OPA plus wavelength tuning of surface-emitting gratings is employed to realize 2-D optical beam steering. The OPA controls the beam steering in the direction perpendicular to the waveguide in the emission array. This direction is designated as the lateral direction in the following. The wavelength tuning controls the beam steering along the waveguide in the emission array. This direction is designated as the longitudinal direction. In the following, lateral beam steering is demonstrated first through controlling the array of phase shifters.

The input signal from the off-chip SGDBR laser has a fixed wavelength at 1539 nm in this case. Our control strategy is to characterize the phase shifters on-site first using the on-chip monitors [19], and then use these characteristics to predict the currents needed for lateral beam sweeping. To do so, first the current injected into the channel 1 phase shifter is fixed at 1 mA and then, the current injected into the channel 2 phase shifter is scanned from 1 to 20 mA. The signal response from the photodiode 1, which monitors the interference between channels 1 and 2, is recorded. The channels and photodiodes are numbered as shown in Fig. 2(a). Then, the current injected into the channel 2 phase shifter is fixed at 1 mA and the current injected into the channel 3 phase shifter is scanned from 1 to 20 mA, and the response from the photodiode 2 is recorded. The above process

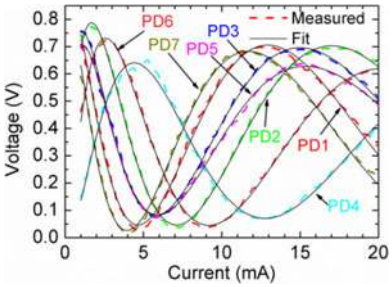

Fig. 8. Measured interference curves through the on-chip monitors and the fitting to a theoretical model.

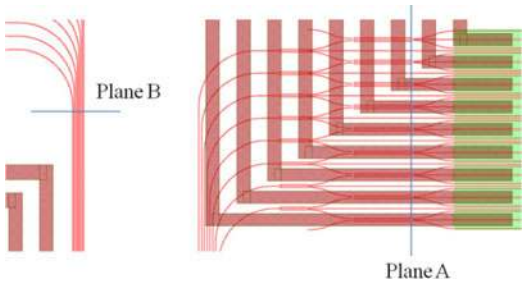

Fig. 9. Blown-up of the layout showing the interference positions.

is repeated until the current injected into the channel 8 phase shifter has been scanned.

All the results are shown in Fig. 8 as dashed lines. These curves clearly show that all the phase shifters are working and 1–20 mA is enough to generate more than 2π phase change. Then, the measured curves are fit to a theoretical model to find out the generated phase by each phase shifter. The model is shown in the following equation:

$$V_{m-1}(I) = C_0\left[1+\exp(-2\alpha)+2\exp(-\alpha)\cos(\Delta\phi)\right]+C_1$$
$$\Delta\phi_m(I) = \Delta\psi + C_2\sqrt{I} + C_3 I,\quad \alpha = C_4(\Delta\phi - \Delta\psi) \qquad (1)$$

where V_{m-1} is the voltage signal generated by the monitor photodiode $(m-1)$, m is from 2 to 8, I is the current injected into the phase shifter m, C_i, i is from 0 to 4, are fitting parameters, α is the loss caused by injected current, $\Delta\psi$ is the initial phase difference when no current is injected, and $\Delta\phi_m$ is the total phase difference between the m-channel and the $(m-1)$-channel. The theoretical model is derived based on the following considerations [20]: the index change induced by current injection is proportional to carrier density in InP-based phase shifters; the relationship between carrier density and current can normally be expressed as $I \propto BN^2 + CN^3$, where N is carrier density, BN^2 accounts for spontaneous emission, and CN^3 account for Auger recombination; spontaneous emission is the dominant term if the carrier density is relatively low, which is why normally phase change is proportional to $I^{1/2}$; in (1), the term $C_3 I$ is added to account for the Auger recombination; the loss coefficient α is proportional to phase change where the proportionality coefficient is related to the linewidth enhancement factor; the derivation of the interference signal V is straightforward by considering a Mach–Zehnder interferometer. The fitted curves are shown in Fig. 8 as solid lines.

Very good fitting effect has been obtained. From the fitting, the differential phase $\Delta\phi_m$ versus current for the channel-m phase shifter has been obtained. The reference of this differential phase is the $(m-1)$-channel with its phase shifter current set at 1 mA, i.e., $\Delta\phi_2(I)$ is relative to channel 1, $\Delta\phi_3(I)$ is relative to channel 2, and so on. To more conveniently use the obtained phase-current relationship of each phase shifter, it would be ideal to change the phase reference of all channels to a unified reference. The simplest way to unify the phase reference is to make all channels refer to channel 1 with its phase shifter current set at 1 mA. This yields the phase-current relationship for channel 2 phase shifter to be $\phi_2(I) = \Delta\phi_2(I)$, and for channel 3 $\phi_3(I) = \Delta\phi_2(I = 1\text{ mA}) + \Delta\phi_3(I)$, and so on. In general, there is

$$\phi_m(I) = \Delta\phi_m(I) + \sum_{2}^{m-1}\Delta\phi_n(I = 1\,\text{mA}),\quad m = 2\ldots 8. \qquad (2)$$

Typical results of the phase-current relationships are similar to what is shown in Fig. 10. Once the phase-current relationship for each phase shifter is known, it is easy to steer the beam, because steering the beam means adding a phase slope to the phased array according to the formula:

$$\phi'_m = \frac{2\pi}{\lambda} d\sin(\theta)(m-1),\quad m = 2\ldots 8 \qquad (3)$$

where ϕ'_m is the phase that the channel-m phase shifter has to generate, d is the waveguide spacing in the emission array, λ is the wavelength, and θ is the angle the beam steers to.

From the phase-current relationship, the current needed to set for each phase shifter can be obtained through interpolation. If the phase that needs to set is beyond the range covered by the obtained phase-current relationship, a modulus of 2π can be used. The first thing attempted was to steer the beam to zero angle in the lateral direction. This means that for each channel, the phase has to be set to zero. When the settings described previously were made, the far-field pattern of the beam is actually not that good. There are two major reasons behind this. One is that the reference position for the differential phase $\Delta\phi_m$ is at the output interface of the 2×1 MMI (Plane A in Fig. 9) instead of the ideal position which is at the entrance of the grating (plane B in Fig. 9).

There are long waveguides between the entrance of the gratings and the output interface of the combiner MMI. These waveguides will cause additional differential phases. In other words, if the differential phase is zero at plane A, it is not at plane B. The second reason is that when the phases at 1 mA phase shifter current are added together [see (2)] in order to unify the phase reference, there is phase error accumulation. For example, if there is some error generated for channel 2 with its phase shifter current at 1 mA, this error will be transferred to channel 3 and channel 4, and so on. In other words, when we say channel 8 has zero phase, it has bigger uncertainties than channel 2. To solve these problems, the seven phase shifter currents $I_m, m = 2\ldots 8$, are adjusted to optimize the far-field pattern at the lateral zero angle using the particle swarm

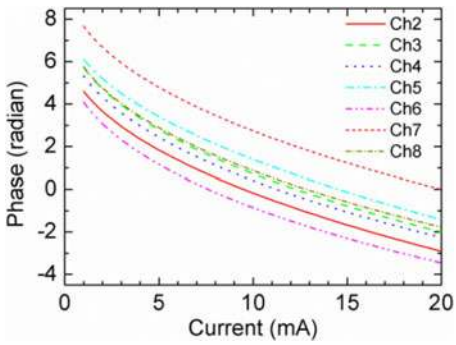

Fig. 10. Phase current curves for phase shifters obtained from the on-chip monitors.

optimization (PSO) algorithm [21]. The channel 1 phase shifter current is fixed at 1 mA. For the optimization, the side-lobe suppression is maximized around the peak at the lateral zero angle within the angle range $[-10^\circ, 10^\circ]$. Once a good beam is obtained—high side lobe suppression and good beam shape—now all the channels have zero phases at the current sets I_m. Thus, the previously found phase-current relationships for all phase shifters are corrected to make sure that all curves have the value of zero at the specific current sets I_m. This can be easily done using the following formula:

$$\phi''_m(I) = \phi_m(I) - \phi_m(I_m), \quad m = 2 \ldots 8. \tag{4}$$

The new phase current curves are the basis of our following beam steering in the lateral direction. Fig. 10 shows these curves.

Fig. 11(a) shows the 3-D plot of the optimized far field at the lateral zero angle. A very elliptical beam can be seen. The FWHM of the beam in the longitudinal direction is about 0.2°, and in the lateral direction, it is about 1.7°. This is determined by the array itself. The emission array has eight channels at the moment. With a 5.5 μm spacing, the array spans a lateral size about 40 μm. Assuming the emission is uniform among all channels, the far-field pattern will be a sinc function with the FWHM of 1.8°, which is in good agreement with the experimental value.

In the longitudinal direction, the grating is 500 μm long. When the grating is etched 20 nm into the 1.3Q upper optical confinement layer, the scattering loss due to grating calculated using the scattering matrix method [22] is only about 0.8 cm^{-1}, much smaller than the intrinsic loss of the waveguide. The grating turns out to be too shallow in terms of scattering power out of the waveguide. So the field (amplitude) inside the waveguide is exponentially decaying at a rate about 1 dB/mm caused by the intrinsic waveguide loss. This determines the far field to be a Lorentzian line shape with the FWHM about 0.16°, which is in agreement with the result we obtained experimentally.

Fig. 12 shows that the beam is steered to different lateral angles using the technique explained earlier. That is, Fig. 10 is used to adjust the phase-shifter currents with no additional reoptimization. It can be seen that good beam shape and good side-lobe suppression around the zeroth diffraction peak have been kept when the beam is steered. The 5.5 μm waveguide spacing determines that the $\pm$1st-order diffraction peaks are

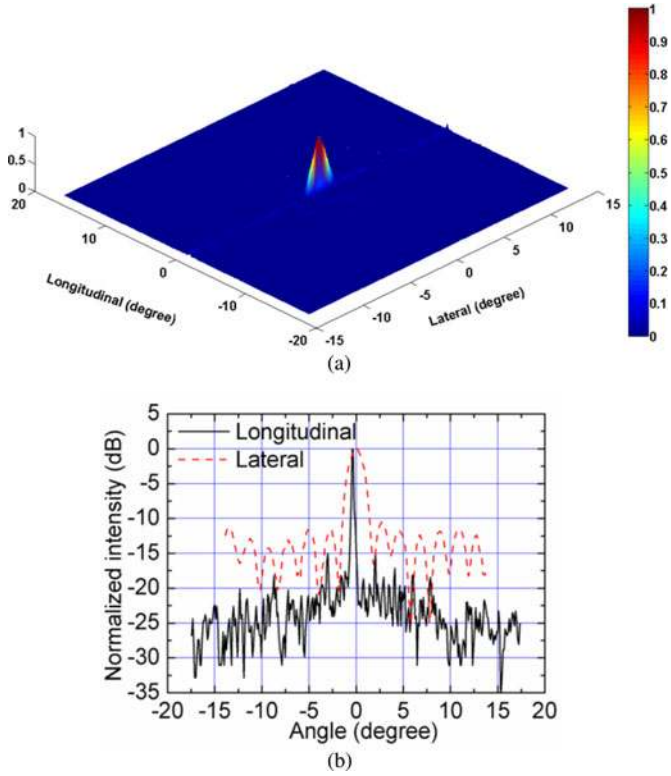

Fig. 11. (a) Three-dimensional plot of the optimized far field at the lateral angle zero. (b) Far field across the peak in the longitudinal and the lateral direction.

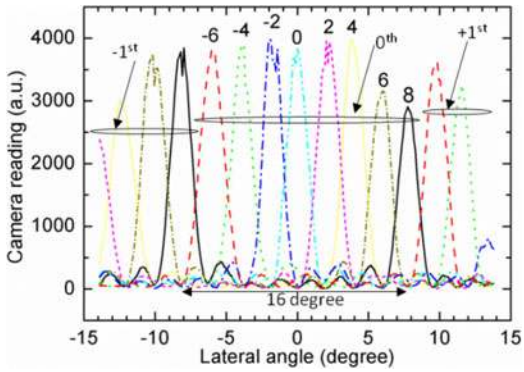

Fig. 12. Far field in the lateral direction for different angles.

about 16° away from the zeroth-order diffraction peak, which can be clearly seen from Fig. 12.

It is known that as long as each phase shifter can generate 2π phase change, the beam can be steered to any angle, not limited to the angles shown in Fig. 12. But a problem is that uniform waveguide spacing, as employed in our emission array, causes periodicity in the far field; i.e., when the zeroth-order diffraction peak is steered out of the range from -8° to 8°, determined by the spacing, the first-order diffraction peaks will enter into this range. This can be seen from Fig. 13 when the beam is further steered to 10° and -10°. The zeroth-order diffraction peaks now overlap with the $\pm$1st-order peaks of -6° and 6°.

In our future work, a nonuniformly spaced array will be used, and this will eliminate all high-order diffraction beams and leave

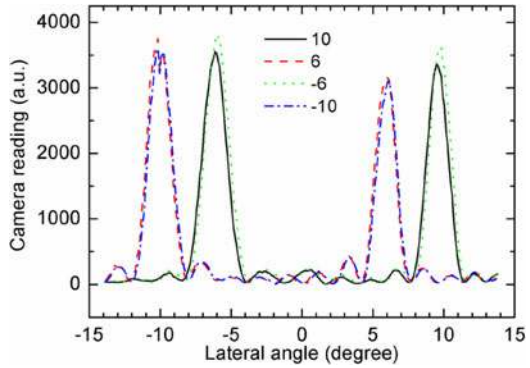

Fig. 13. Far field in the lateral direction for the lateral angles of $-10°$, $-6°$, $6°$, and $10°$.

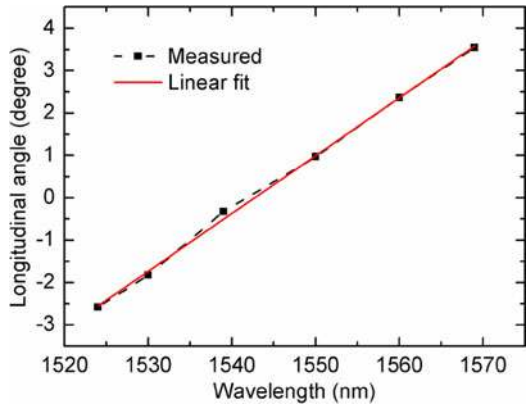

Fig. 14. Beam position in the longitudinal direction versus wavelength.

only the zeroth-order diffraction beam, so this problem will not exist anymore.

D. Beam Steering Controlled by Wavelength Tuning

Longitudinal beam steering is demonstrated by changing the input wavelength. The emission angle relies on the input wavelength through the following relation:

$$\sin(\theta) = \frac{\lambda}{\Lambda} - n_{\text{eff}} \tag{5}$$

where Λ is the pitch of the grating and n_{eff} is the effective index of the waveguide. For small emission angles, it can be approximated as

$$\theta = \frac{\lambda}{\Lambda} - n_{\text{eff}}. \tag{6}$$

The efficiency of the beam steering in terms of $d\theta/d\lambda$ is

$$\frac{d\theta}{d\lambda} = \frac{n_g}{\lambda}\frac{180}{\pi} \tag{7}$$

where n_g is the group index; $d\theta$ has the units of degrees. Our waveguide has a group index around 3.75, so the efficiency is expected to be 0.14°/nm.

Fig. 14 shows the experimentally obtained beam position in the longitudinal direction versus wavelength. The slope is 0.14°/nm in agreement with the theoretical prediction. When the input wavelength is varied to steer the beam longitudinally,

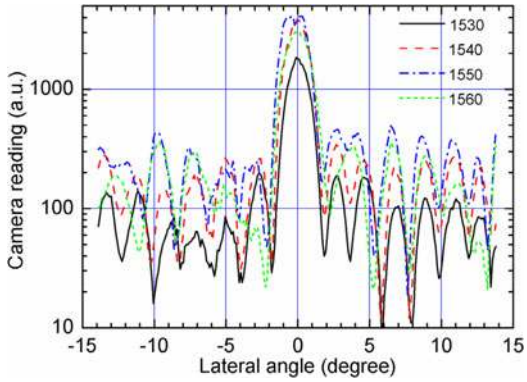

Fig. 15. Far field in the lateral direction for different wavelengths; the beam steers to the lateral angle of zero degree.

it would be good that there is no need to reset the phase shifter current in order to keep the beam in a good shape. This is, however, difficult because very long deep ridge waveguides especially long bends in the channel have been used, and there are also SOAs in the channel. In the layout, all channels are designed to be exactly the same. "Exactly" means that first the positions of all the SOAs relative to the splitters are the same so that the input power to the SOAs is ideally to be the same; second, the same bends are used in each channel, so their effects are ideally to cancel with each other. In Fig. 15, the far field in the lateral direction is shown for different wavelengths and for the same lateral angle, 0°.

When wavelength changes, the beam power also changes. This is caused by the limited gain-bandwidth of the SOAs. For 1550-nm wavelength, the camera is a little saturated so that the peak looks cutoff in the figure. However, it can be seen that the beam continues to have a relatively good shape, good side-lobe suppression, and beamwidth. Of course, careful fabrication is still needed to reduce variations among channels even with a very cautious design.

For some of our devices, some far-field variations are still seen when changing wavelength without resetting the phase shifter currents. Even for the devices with relatively good far-field patterns, improvement is still desired. Reasons for these variations include bend losses, which can add about 3 dB due to their length of approximately 1.5 mm. The layout is also pretty complex as seen from Fig. 1, and this will become a hurdle if scaling up to a larger array with significantly more channels. Thus, equal channel length designs may not worth the additional loss and layout complexities required, given that the promised simplicity in operation may not provide the needed performance. Simpler, short, low waveguide loss designs may be better, especially for larger arrays, although these would require large phase-shifter current changes for each wavelength. The control circuits may not be much more complex than required for small changes, however.

E. Two-Dimensional Optical Beam Steering

To carry out 2-D optical beam steering, the phase shifter control and the input wavelength control need to be combined.

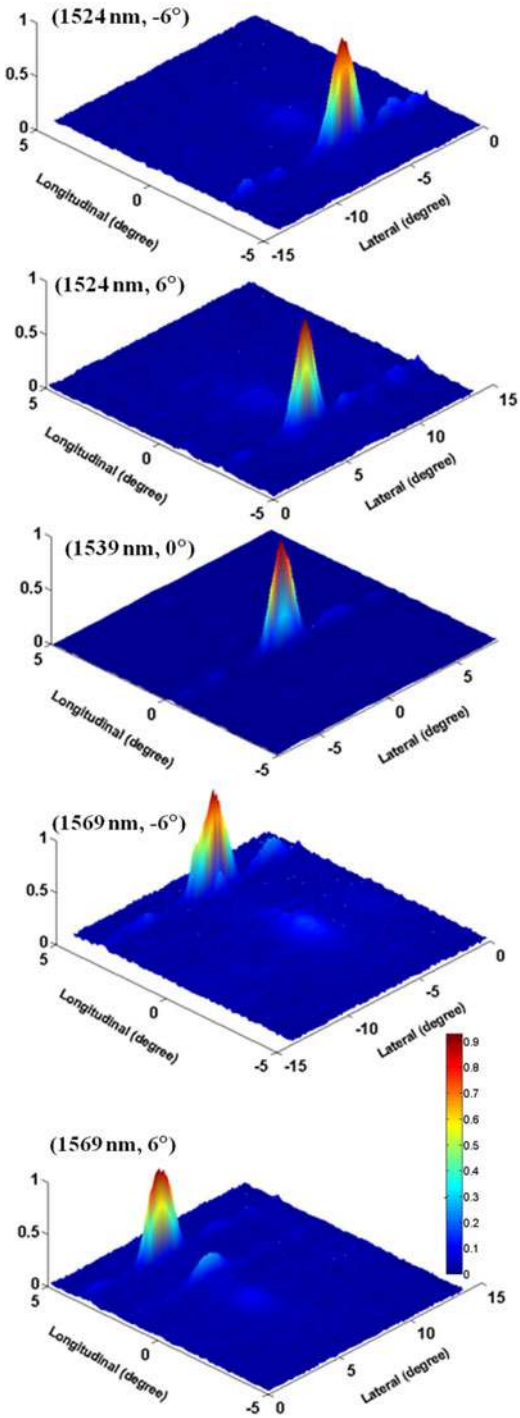

Fig. 16. Three-dimensional plot of the far-field patterns for some critical angles in the 2D plane.

The process is relatively simple: first optimize the far field for the wavelength of 1539 nm pointing at the lateral angle of zero degrees using the PSO algorithm; then spread the controls across different lateral angles using those phase-current relationships of phase shifters (see Fig. 10); and then spread the controls across the 2-D plane by changing wavelength (see Fig. 14). Initially, no further far-field optimizations are done for any angles. Fig. 16 shows a 3-D plot of the far-field patterns for some critical angles of the 2-D plane. Although relatively good, improvements can be done by using the PSO algorithm around the current setting that is already available from the plots. When the input wavelength is away from the gain peak, for some lateral angles (specific phase shifter current settings), the influence from the reflections of the gratings (1569 nm, 6° in Fig. 16) is seen. In the future, we will take measures to reduce the grating reflections such as laterally angling the interface of the grating tooth relative to the waveguide, angling the emission in the longitudinal direction by pushing the Bragg reflection wavelength far out of the gain window, etc.

In the following, some comments on how to further improve the beam steering angle range, i.e., the total field of view (TFOV) are made. What has been shown here is 12° in the lateral direction and 6° in the longitudinal direction. For a larger angle in the longitudinal direction, a larger wavelength tuning range can be used, or lenses can be employed to magnify the angle [23]. The former method is very challenging. Considering the available tuning range of the monolithic integrated tunable laser and the SOA effective gain bandwidth, a tuning range about 80 nm can most likely be achieved [24]. This will yield a TFOV of about 11°. To get an even larger TFOV, lens magnification has to be used. When using lenses to magnify the TFOV, the beamwidth is also increased by the same amount, which means that to satisfy the requirement on the final beamwidth, the original beamwidth has to be reduced by the same amount. This can be achieved by using longer and shallower gratings.

For the lateral direction, there is no limitation to the steering angle if a 2π phase change can be achieved for each phase shifter. However, there is another limitation which is the side-lobe suppression. Because the waveguide spacing has to be relatively large (for low loss and independent phase control), high side-lobe suppression is difficult to be achieved in a large angle range, but it is possible to be realized in a rather small angle range. For example, it is difficult to realize 20 dB side-lobe suppression in a 45° angle range, but it is not that hard for a 10° angle range by simply using nonuniformly spaced arrays. Any emission beyond this relatively smaller angle range is blocked. Then, lenses are used to magnify the steering angle range. In this way, one can achieve large steering angle and high side-lobe suppression simultaneously. So to achieve good side-lobe suppression within a large angle range, the best way is probably still to use lens magnification. In other words, lenses are employed to magnify the TFOV in both directions. For the same reason to make the beamwidth still within the same metric, a larger array (more channels) has to be used. This, however, involves a much bigger effort than increasing the grating length, because more channels means much larger integration and many more controls. Fortunately, only one dimension (lateral) requires individual phase controls.

F. Fast Optical Beam Steering

One big advantage of electronically controlled beam steering is that the beam can potentially be steered to different directions very fast. In our situation, the steering speed is limited by the phase shifter bandwidth and the tuning speed of the tunable

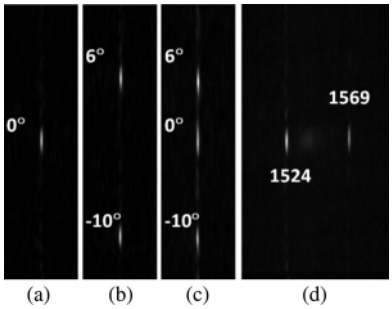

Fig. 17. Camera images of the far-field spot for two lateral angles without (a), (b) and with (c) fast beam steering. (d) Far-field spot when wavelength is fast switching.

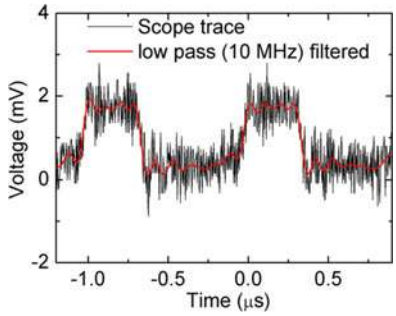

Fig. 18. Oscilloscope trace from the detector placed above the PIC.

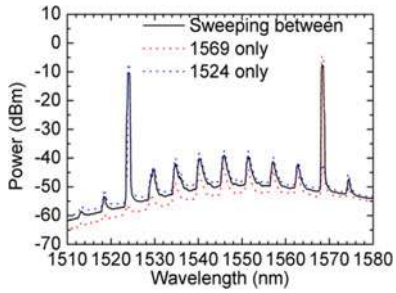

Fig. 19. Laser output spectra for two wavelengths and for fast switching between them.

laser. The current-injection phase shifters used in our PIC are 200 μm long, so even considering the carrier lifetime, the bandwidth can approach the gigahertz range. The SGDBR tunable laser can potentially have a few nanoseconds tuning speed [14]. So our PIC can potentially have a very fast beam steering speed. In the following, some preliminary tests for fast beam steering based on our PIC are demonstrated. We are primarily limited by the electrical connections to PIC, which only allows megahertz modulation. However, custom drive circuits in fabrication should soon enable the predicted $\sim$100 MHz speed. If phase shifters employing the electrooptical effect and traveling wave electrodes were used, lateral steering bandwidths in the tens of gigahertz would be possible [25].

Here, fast beam steering in the lateral direction is reported. Seven function generators (FGs) are employed to control seven phase shifters. These FGs are synchronized by using one of them as the master: its clock output is used to synchronize all the other FGs. Series termination resistors of 50 Ω are connected to the phase shifters. Square waves of 1 MHz with 50% duty cycle are employed. The dc offset and amplitude of the square wave from each FG is optimized using the previous dc results for good far-field spots. The FGs are used as voltage sources and the dc offset is changed to scan the *I–V* curve of the phase shifters. The current is found by monitoring the voltage drop on the 50-Ω series resistance. Then, the optimal voltages can be decided from the required currents (datasets already established from previous experiments). Two lateral angles are selected: one is 0° and the other one is -10°. The wavelength is fixed at 1539 nm. Good beams are demonstrated at both excursions of the square wave, demonstrating more than sufficient PIC response bandwidth.

Fig. 17(a) and (b) shows the camera images of the far-field spots for the two states. When the modulation is on, the beam is switched between the two directions at 1 MHz speed which is much faster than the frame rate of the camera, so two states on the camera are observed simultaneously. To check if the beam is really switching between the two states, a photodetector is placed on top of the PIC to try to capture the upward emission. The signal of the detector is maximized when the beam is pointing at 0°. When the modulation is on, the detector signal is monitored by an oscilloscope.

The result is shown in Fig. 18. A very weak signal has been captured, so it is very noisy on the real-time oscilloscope. However, a clear indication of 1 MHz sweeping speed can be seen. So, fast steering between two angles in the lateral direction through controlling the phase shifters has been demonstrated. The speed is $10^\circ/0.5\ \mu\text{s} = 2 \times 10^7\ ^\circ/\text{s}$. We believe that by using proper electrical connections and by using faster current drivers, the PIC should be able to achieve much higher steering speeds as mentioned earlier.

In the longitudinal dimension, fast beam steering is achieved by quickly changing the output wavelength of the tunable laser. To do this, the back mirror current of the SGDBR laser is fixed. The front mirror in series connection with a 50-Ω resistance is driven by an FG also by a square wave with 50% duty cycle at 1 MHz. The dc offset and amplitude of the square wave are optimized to select two output wavelengths. The laser output spectra at these two specific states are shown in Fig. 19.

When the laser output is quickly switching between these two states at 1 MHz, the spectrum analyzer captures the two output wavelengths at the same time. The same happens to the camera which captures the two far-field spots corresponding to the two wavelengths simultaneously, as shown in Fig. 17(d). To check if the wavelength is really quickly switching, the output of the laser is tapped and then passes through a narrow-band optical filter tuned to align with the 1529-nm wavelength. The output after the filter is monitored by a TIA integrated photodiode. The response from the detector is recorded by the same oscilloscope with the trace shown in Fig. 20. Clearly a switching speed of 1 MHz has been demonstrated. Considering the two states are 6° apart (see Fig. 14) in the longitudinal direction, $1.2 \times 10^7\ ^\circ/\text{s}$ steering speed has thus been achieved. There is still margin to improve.

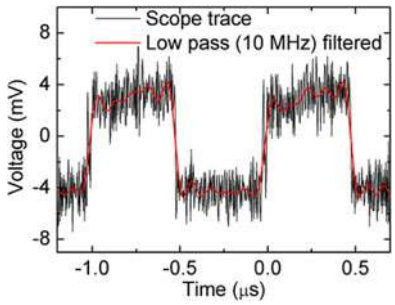

Fig. 20. Oscilloscope trace from the photodiode that monitors the wavelength switching.

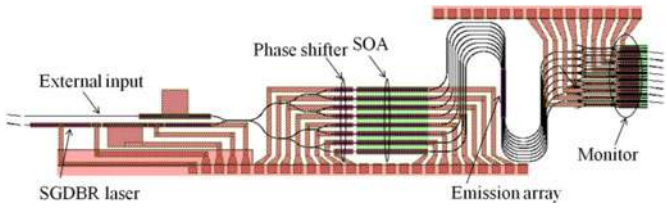

Fig. 21. Layout of the PIC with on-chip SGDBR laser.

The SGDBR laser has demonstrated a few nanoseconds tuning speed over a wide wavelength range [14].

V. SGDBR Laser Integrated On-Chip

More recently, we have integrated the widely tunable SGDBR laser with the PIC shown in Fig. 1. The new layout is shown in Fig. 21.

Compared with the previous PIC layout shown in Fig. 1, the first splitter has been changed from a 1×2 MMI to a 2×2 MMI. This allows us to add one input as the on-chip SGDBR widely tunable laser. From the left to right, the laser includes the back mirror section, phase section, gain section, front mirror section, and the SOA section. Processing the new PIC is similar except that two steps of etching are used to form the sampled gratings used for the SGDBR laser and the surface-emitting gratings. The sampled gratings are etched 80 nm into the upper optical confinement layer, so much deeper than the surface-emitting gratings (20 nm). Another change for the new PIC is that phase shifters are placed in front of channel SOAs. This is to employ the SOA saturations to reduce the variations of the power entering into the emission array when phases are adjusted by injecting currents into the phase shifters.

What has been done first is to characterize the on-chip SGDBR laser. Fig. 22 shows the spectra of the on-chip SGDBR laser output from the back mirror. Here, only supermodes of the laser are shown. They are selected by tuning the front and back mirror sections but leaving the phase section unbiased. A total tuning range close to 30 nm is expected from this on-chip tunable laser.

Then, the beam is steered in the longitudinal direction by tuning the on-chip tunable laser. Fig. 23(a) shows the 3-D plot of the far-field spots for different wavelengths superimposed together. The beam steers to zero degree in the lateral direction. Fig. 23(b) shows the far-field distribution across the peak in the

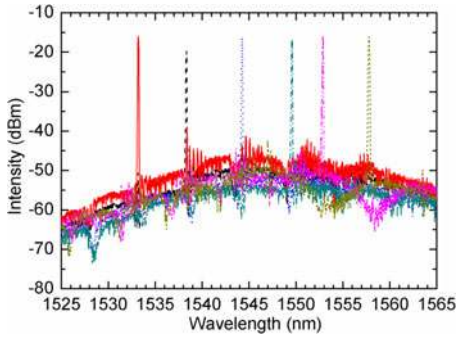

Fig. 22. Spectra of the on-chip SGDBR laser output from the back mirror.

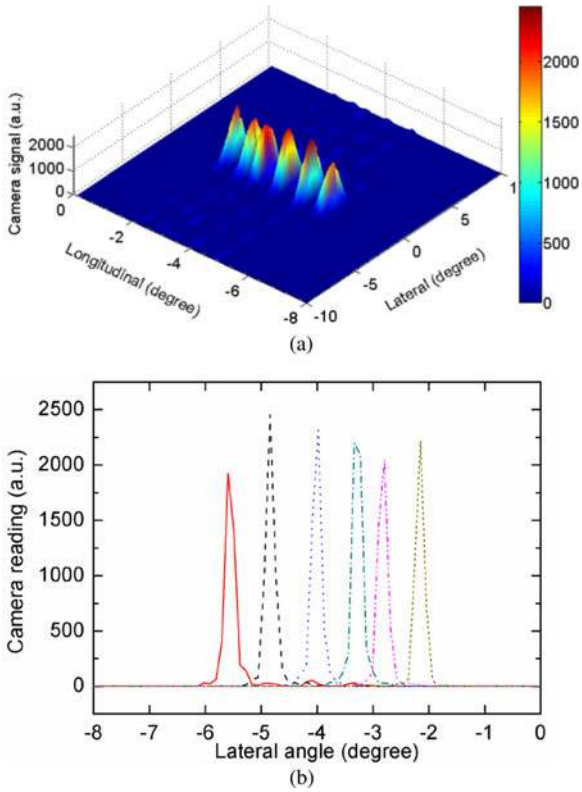

Fig. 23. (a) Three-dimensional plot of the far-field pattern for different wavelengths superposed together. (b) Far field across the peak in the longitudinal direction.

longitudinal direction. Very narrow (FWHM about 0.2° similar to previous results) and clean peaks are seen.

Then, the wavelength of the SGDBR laser is fixed at 1538 nm and the beam is steered in the lateral direction by using the array of phase shifters. Fig. 24(a) shows the 3-D plot of the far field patterns for lateral angles from $-5°$ to $5°$ with a step of $2°$ superimposed together and (b) shows the far-field distribution across the peak in the lateral direction. The far-field in the lateral direction is broad so they overlap with each other when superimposed together. The FWHM of the beam in the lateral direction is about $2°$, so similar to previous results as well.

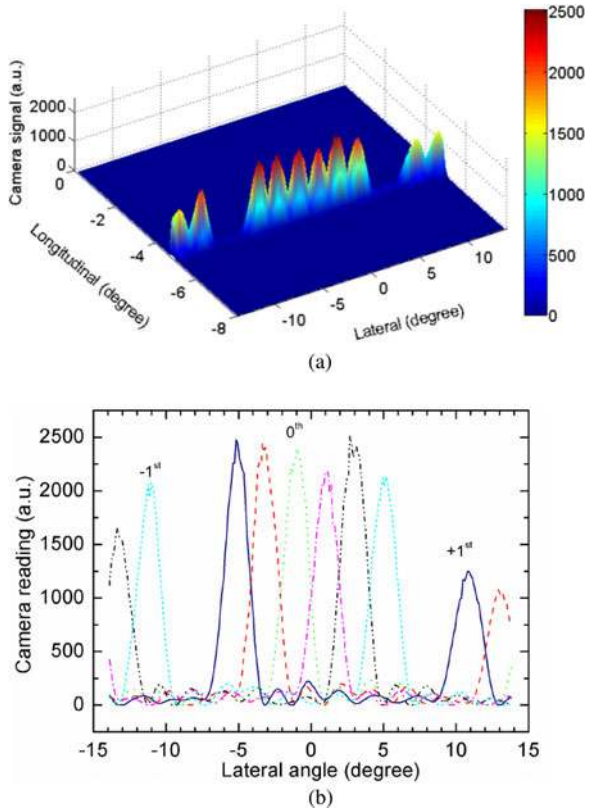

Fig. 24. (a) Three-dimensional plot of the far-field patterns. (b) Far-field distribution in the lateral direction for lateral angles from -5° to 5° with a step of 2° superimposed together.

VI. Conclusion

In summary, 2-D optical beam steering with an InP PIC using a 1-D OPA and wavelength tuning with surface-emitting gratings has been demonstrated. The on-chip monitors have made the 1-D OPA calibration and control easier. In general, because of fewer control elements, controlling this PIC for 2-D optical beam steering is going to be much easier than the method that uses a 2-D array of elements, such as VCSEL array or MEMS array. The tunable SGDBR laser has been successfully integrated and 2-D beam steering has been demonstrated with this on-chip tunable laser source as well. Looking forward to obtaining even larger beam steering angles and higher side-lobe suppressions, the best way is to use lens magnification as discussed in this paper. However, to make the beamwidth still within the metric a larger circuit: more channels and longer gratings must be used. More channels are also helpful to increase the output power as long as the thermal issue is well managed. So the PIC demonstrated in the paper has the ability to scale up and is promising toward practical applications.

References

[1] P. F. McManamon, T. A. Dorschner, D. L. Corkum, L. J. Friedman, D S. Hobbs, M. Holz, S. Liberman, H. Q. Nguyen, D. P. Resler, R. C. Sharp, and E. A. Watson, "Optical phased array technology," *Proc. IEEE*, vol. 84, no. 2, pp. 268–298, Feb. 1996.

[2] D. P. Resler, D. S. Hobbs, R. C. Sharp, L. J. Friedman, and T. A. Dorschner, "High-efficiency liquid-crystal optical phased-array beam steering," *Opt. Lett.*, vol. 21, no. 9, pp. 689–691, May 1996.

[3] F. Vasey, F. K. Reinhart, R. Houdre, and J. M. Stauffer, "Spatial optical beam steering with an AlGaAs integrated phased array," *Appl. Opt.*, vol. 32, no. 18, pp. 3220–3232, Jun. 1993.

[4] [Online]. Available at http://en.wikipedia.org/wiki/Active_electronically_scanned_array

[5] G. Hergenhan, B. Lucke, and U. Brauch, "Coherent coupling of vertical-cavity surface-emitting laser arrays and efficient beam combining by diffractive optical elements: concept and experimental verification," *Appl. Opt.*, vol. 42, no. 9, pp. 1667–1680, Mar. 2003.

[6] D. F. Siriani and K. D. Choquette, "Electronically controlled two-dimensional steering of in-phase coherently coupled vertical-cavity laser arrays," *IEEE Photon. Technol. Lett.*, vol. 23, no. 3, pp. 167–169, Feb. 2011.

[7] A. Tuantranont, V. M. Bright, J. Zhang, W. Zhang, J. A. Neff, and Y. C. Lee, "Optical beam steering using MEMS-controllable microlens array," *Sens. Actuators A*, vol. 91, no. 3, pp. 363–372, Jul. 2001.

[8] F. Xiao, W. W. Hu, and A. S. Xu, "Optical phased-array beam steering controlled by wavelength," *Appl. Opt.*, vol. 44, no. 26, pp. 5429–5433, Sep. 2005.

[9] K. V. Acoleyen, W. Bogaerts, J. Jagerska, N. L. Thomas, R. Houdre, and R. Baets, "Off-chip beam steering with a one-dimensional optical phased array on silicon-on-insulator," *Opt. Lett.*, vol. 34, no. 9, pp. 1477–1479, May 2009.

[10] W. H. Guo, P. R. A. Binetti, C. Althouse, A. Bhardwaj, J. K. Doylend, H. P. M. M. Ambrosius, L. A. Johansson, and L. A. Coldren, "InP photonic integrated circuit for 2D optical beam steering," presented at the Proc. IEEE Photon., Arlington, VA, 2011, Post-deadline Paper.

[11] J. K. Doylend, M. J. R. Heck, J. T. Bovington, J. D. Peters, L. A. Coldren, and J. E. Bowers, "Two-dimensional free-space beam steering with an optical phased array on silicon-on-insulator," *Opt. Exp.*, vol. 19, no. 22, pp. 21595–21604, Oct. 2011.

[12] S. C. Nicholes, M. L. Masanovic, B. Jevremovic, E. Lively, L. A. Coldren, and D. J. Blumenthal, "An 8×8 InP monolithic tunable optical router (MOTOR) packet forwarding chip," *J. Lightw. Technol.*, vol. 28, no. 4, pp. 641–650, Feb. 2010.

[13] L. A. Coldren, "Monolithic tunable diode lasers," *IEEE J. Sel. Topics Quantum Electron.*, vol. 6, no. 6, pp. 988–999, Nov. 2000.

[14] J. E. Simsarian, M. C. Larson, H. E. Garrett, H. Xu, and T. A. Strand, "Less than 5-ns wavelength switching with an SG-DBR laser," *IEEE Photon. Technol. Lett.*, vol. 18, no. 4, pp. 565–567, Feb. 2006.

[15] W. H. Guo, P. R. A. Binetti, C. Althouse, L. A. Johansson, and L. A. Coldren, "InP photonic integrated circuit with on-chip tunable laser source for 2D optical beam steering," presented at the Opt. Fiber Commun. Conf., Anaheim, CA, 2013, Paper OTh3I.7.

[16] E. J. Skogen, J. S. Barton, S. P. Denbaars, and L. A. Coldren, "A quantum-well-intermixing process for wavelength-agile photonic integrated circuits," *IEEE J. Sel. Topics Quantum Electron.*, vol. 8, no. 4, pp. 863–869, Jul. 2002.

[17] J. S. Parker, E. J. Norberg, R. S. Guzzon, S. C. Nicholes, and L. A. Coldren, "High verticality InP/InGaAsP etching in Cl2/H2/Ar inductively coupled plasma for photonic integrated circuits," *J. Vac. Sci. Technol. B*, vol. 29, no. 1, pp. 011016–011020, Jan. 2011.

[18] S. Park, S. H. Song, C. H. Oh, and P. S. Kim, "Ray-optical determination of the coupling coefficient of grating waveguide by use of the rigorous coupled-wave theory," *J. Lightw. Technol.*, vol. 19, no. 1, pp. 120–125, Jan. 2001.

[19] W. H. Guo, P. R. A. Binetti, C. Althouse, H. P. M. M. Ambrosius, L. A. Johansson, and L. A. Coldren, "InP photonic integrated circuit with on-chip monitors for optical beam steering," presented at the Int. Semicond. Laser Conf., San Diego, CA, Oct. 2012, Paper MA6.

[20] L. A. Coldren, S. W. Corzine, and M. L. Mashanovitch, *Diode Lasers and Photonic Integrated Circuits*, 2nd ed. New York: Wiley, Mar. 2012.

[21] J. Robinson and Y. Rahmat-Samii, "Particle swarm optimization in electromagnetics," *IEEE Trans. Antennas Propag.*, vol. 52, no. 2, pp. 397–407, Feb. 2004.

[22] Q. Y. Lu, W. H. Guo, R. Phelan, D. Byrne, J. F. Donegan, P. Lambkin, and B. Corbett, "Analysis of slot characteristics in slotted single-mode semiconductor lasers using the 2-D scattering matrix method," *IEEE Photon. Technol. Lett.*, vol. 18, no. 24, pp. 2605–2607, Dec. 2006.

[23] W. H. Guo, P. R. A. Binetti, C. Althouse, H. P. M. M. Ambrosius, L. A. Johansson, and L. A. Coldren, "Improved performance of optical beam steering through an InP photonic integrated circuit," presented at the Conf. Lasers Electro-Opt., San Jose, CA, May 2012, Paper CW1 K.2.

[24] B. Mason, J. Barton, G. A. Fish, L. A. Coldren, and S. P. DenBaars, "Design of sampled grating DBR lasers with integrated semiconductor optical amplifiers," *IEEE Photon. Technol. Lett.*, vol. 12, no. 7, pp. 762–764, Jul. 2000.

[25] R. Fabian, W. Pease, D. A. B. Miller, and T. H. Lee, "High-speed optical beam-steering based on phase-arrayed waveguides," *J. Vac. Sci. Technol. B: Microelectron. Nanometer Struct.*, vol. 26, no. 6, pp. 2124–2126, Nov. 2008.

Weihua Guo received the B.Sc. degree in physics from Nanjing University, Nanjing, China, in 1998, and the Ph.D. degree from the Institute of Semiconductors, Chinese Academy of Sciences, Beijing, China, in 2004. His Ph.D. research was focused on simulation and fabrication of optical microcavities and semiconductor optical amplifiers.

From September 2004 to October 2010, he was a Postdoctoral Researcher at the Department of Physics, Trinity College Dublin, Dublin, Ireland, where he did research on various topics such as optical performance monitoring techniques and tunable integrated sources for coherent wavelength division multiplexing systems. In November 2010, he joined the Department of Electrical and Computer Engineering, University of California Santa Barbara, Santa Barbara, as an Assistant Project Scientist. His current research interests include using InP photonic integrated circuits to realize novel functions.

Pietro R. A. Binetti received the Ph.D. degree in electrical engineering from the COBRA Research Institute, Eindhoven University of Technology, Eindhoven, The Netherlands, in 2009.

He is currently a Postdoctoral Researcher at the University of California Santa Barbara, Santa Barbara. His research interests include design, fabrication, and characterization of photonic integrated circuits for analog and digital applications.

Chad Althouse received the B.S. degree from Penn State University, University Park, in 2007, and the M.S. degree from the University of California Santa Barbara (UCSB), Santa Barbara, in 2012, both in materials. As a Ph.D. student in material science at UCSB, he designed, fabricated, and tested photonic integrated circuits including integrated optical isolators and injection-locked tunable lasers for high-speed communication.

He is currently a Process Engineer at Innovative Micro Technology, Goleta, CA, USA, where he is working to develop microelectromechanical systems technology. He has worked on various other government-funded research projects throughout his studies at Penn State University and UCSB.

Milan L. Mašanović (S'98–M'04) received the Dipl.Ing. degree from the School of Electrical Engineering, University of Belgrade, Belgrade, Yugoslavia, in 1998, and the M.S. and Ph.D. degrees from the University of California Santa Barbara, Santa Barbara, in 2000 and 2004, respectively, all in electrical engineering.

He is currently a Research Scientist at the University of California Santa Barbara. He is also a founder of Freedom Photonics, a photonic integration company in Santa Barbara, CA. He is the author or coauthor of more than 70 research papers. His current research interests include InP photonic integration related to applications in packet-switched optical networks.

Dr. Mašanović was the recipient of the 2003 Best Student Paper Award at the Indium Phosphide and Related Materials Conference and the 2004 IEEE Lasers and Electro-Optics Society Graduate Student Fellowship Award.

Huub P. M. M. Ambrosius received the Ph.D. degree in chemistry from the Catholic University of Nijmegen (now Radboud University), Nijmegen, The Netherlands, in 1981.

He then joined Philips Research Labs in Eindhoven, The Netherlands, working on III/V technology for lasers and photodetectors. From September 1987 to September 1988, he worked as ex-pat at the Philips Research Lab in Limeille-Brevannes (France) working on the first planetary MOVPE reactor. After the acquisition of the Philips Optoelectronic Centre by Uniphase (later JDS Uniphase) in 1998 he was Engineering Manager in the Waferfab until JDS Uniphase closed down the facility in Eindhoven in 2004. In 2005, he cofounded Cedova BV in Eindhoven, and in 2009, he joined the Optoelectronic Devices Group at the Eindhoven University of Technology, Eindhoven, responsible for the cleanroom activities and the technology. Recently, he became Managing Director of NanoLab@TU/e, the cleanroom facility of the Eindhoven University of Technology.

Leif A. Johansson (M'04) received the Ph.D. degree in engineering from University College London, London, U.K., in 2002.

He is currently a Research Scientist with the University of California Santa Barbara, Santa Barbara. His current research interests include design and characterization of integrated photonic devices for analog and digital applications and analog photonic systems and subsystems.

Larry A. Coldren (S'67–M'72–SM'77–F'82) received the Ph.D. degree in electrical engineering from Stanford University, Stanford, CA, in 1972.

He is currently the Fred Kavli Professor of Optoelectronics and Sensors at the University of California Santa Barbara (UCSB), Santa Barbara. After 13 years in the research area at Bell Laboratories, he joined UCSB in 1984, where he is currently with the Department of Materials and the Department of Electrical and Computer Engineering. In 1990, he cofounded Optical Concepts, later acquired as Gore Photonics, to develop novel vertical-cavity surface-emitting laser (VCSEL) technology. In 1998, he cofounded Agility Communications, later acquired by JDSU, to develop widely tunable integrated transmitters. At Bell Labs, he initially worked on waveguided surface-acoustic-wave signal processing devices and coupled-resonator filters. He later developed tunable coupled-cavity lasers using novel reactive-ion etching technology that he created for the then new InP-based materials. At UCSB, he continued work on multiple-section tunable lasers, in 1988, inventing the widely tunable multielement mirror concept, which is now used in some JDSU products. Near this same time period, he also made seminal contributions to efficient VCSEL designs that continue to be implemented in practical devices to this day. More recently, his group has developed high-performance InP-based photonic integrated circuits as well as high-speed VCSELs, and they continue to advance the underlying materials growth and fabrication technologies. He has authored or coauthored more than a thousand journal and conference papers, seven book chapters, and one textbook and has been issued 64 patents. He has presented dozens of invited and plenary talks at major conferences.

Dr. Coldren is a Fellow of the Optical Society of America, the Institution of Electrical Engineers, and a member of the National Academy of Engineering. He was a recipient of the 2004 John Tyndall and 2009 Aron Kressel Awards.